Accurate numerical solutions to the forward problem of local helioseismology

Michael Leguèbe[1], Chris S. Hanson[1], Damien Fournier[2], Aaron C. Birch[1] & Laurent Gizon[1,3]

[1]Max-Planck-Institut für Sonnensystemforschung, Göttingen, Germany
[2]Institut für Numerische und Angewandte Mathematik, Göttingen, Germany
[3]Institut für Astrophysik, Georg-August-Universität Göttingen, Germany

in collaboration with **Inria team Magique3D**,
Inria Bordeaux Sud-Ouest, France

We compute acoustic Green's functions in an axisymmetric solar background model, which may include a meridional flow and differential rotation. The wave equation is solved in the frequency domain using a finite element solver. A transparent boundary condition for the waves is implemented in the chromosphere, which represents a great improvement in computational efficiency compared to implementations based on 'sponge layers'. We perform various convergence studies that demonstrate that wave travel times can be computed with an accuracy of 0.001 s. This high level of numerical accuracy is required to interpret travel times in the deep interior, and is achieved thanks to a refined mesh in the near surface layers and around the source of excitation. The wave solver presented here lays the ground for future iterative inversion methods for flows in the deep solar interior.

This poster is continued from Chris Hanson's *'Computational Local Helioseismology in the Frequency Domain'* poster.

Computational mesh, boundary conditions

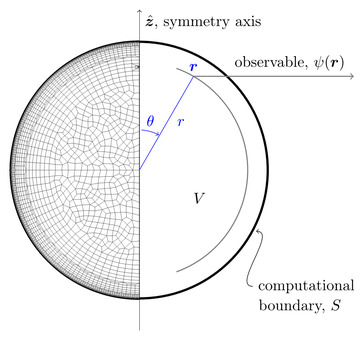

Figure 5: Geometrical setup and mesh used in Montjoie for solving the wave equation.

The computational domain is descretized with a mesh adapted to the steep variations of the solar background (Fig. 5). For $r > 0.7R_\odot$, the cell height is set to be equal to the radial wavelength

$$\lambda_r = 2\pi \left(\frac{\omega_{\rm mesh}^2}{c^2} - \frac{\ell_{\rm mesh}(\ell_{\rm mesh}+1)}{R_\odot^2} \right)^{-1/2}, \qquad (11)$$

where $\ell_{\rm mesh} = 15$ is the minimum angular degree that we want to study and $\omega_{\rm mesh}$ is 9 mHz. A Neumann boundary condition (BC) is imposed on the rotation axis in order to be compatible with the axisymmetric setup.

Atmosphere extension. On the computational boundary S, we first implement a Sommerfeld-like BC

$$\partial_{\boldsymbol{n}} G_\omega = \mathrm{i}k_{\boldsymbol{n}} G_\omega \text{ on } S, \qquad (12)$$

which is valid if the background is locally uniform at the boundary. To be able to use this BC, we extend the density and sound speed profiles up to 4 Mm above the photosphere. After a smooth transition region between 500 km (end of the standard model) and 2 100 km, the background is assumed to be uniform. The acoustic cut-off frequency, defined by:

$$\omega_{\rm ac}^2 := \sqrt{\rho} c^2 \frac{1}{r^2} \partial_r \left(r^2 \partial_r \frac{1}{\sqrt{\rho}} \right), \qquad (13)$$

is then equal to zero in a layer below the computational boundary (Fig. 6). In this layer, waves with frequencies above ~5.3 mHz propagate out until they are attenuated by the boundary.

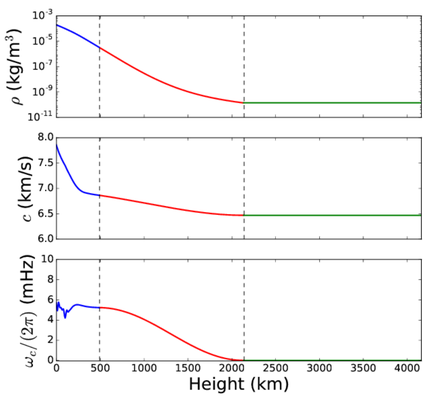

Figure 6: Extension of the density (top) and sound-speed (middle) profiles. Bottom panel: resulting acoustic cut-off frequency.

Accuracy of the solver in a solar-like context

Green's function comparison To adress the accuracy of our forward solver, we measure the convergence of Green's functions $G^{(p)}$ computed on the mesh shown in Fig. 5 with polynomials of order $2 \leqslant p \leqslant 12$ towards a solution $G_{\rm ref}$. As we cannot determine the exact solution to our problem, we use for $G_{\rm ref}$ a numerical solution to Eq. (1) computed on a highly refined mesh with high-order discretization (order 13).

As shown in Fig. 7, the relative difference between the imaginary parts of $G^{(p)}$ and $G_{\rm ref}$ reaches a value of $\sim 10^{-5}$ for the order of discretization $p = 10$ that we use in practice.

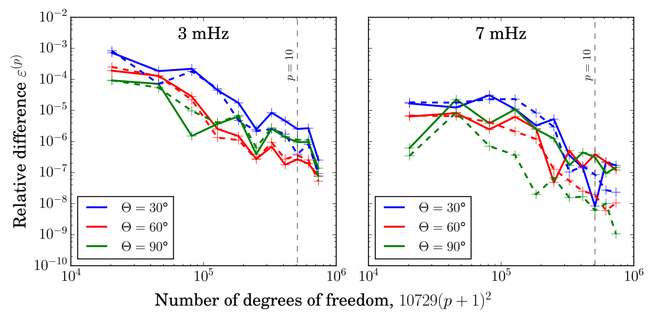

Figure 7: Relative difference of imaginary parts of Green's functions computed with order of discretization p and a reference solution, for separation distances $\Theta = 30°$, $60°$ and $90°$, and frequencies $\omega/2\pi = 3$ mHz and 7 mHz. Solid lines indicate simulation without flow, and dashed lines computations including a meridional flow cell in the background (see [3] for a description of the flow cell). 10 729 is the number of cells in the mesh with extended atmosphere.

Travel time accuracy. We now compute compute the travel-times $\delta\tau^{(p)}$ induced by solving Eq. (1) with orders of discretization $2 \leqslant p \leqslant 12$, for waves originating from the pole:

$$\delta\tau^{(p)} = \int W_{\rm ref}^*(C^{(p)} - C_{\rm ref})\, \mathrm{d}\omega. \qquad (14)$$

$C^{(p)}$ (resp. $C_{\rm ref}$) is the cross-covariance computed from $G^{(p)}$ (resp. $G_{\rm ref}$), and $W_{\rm ref}$ a weighting function deduced from $C_{\rm ref}$ [see 2]. Green's functions were computed for a Nyquist frequency of 8.33 mHz with a frequency resolution of 3.3 μHz, and a constant damping $\gamma/2\pi = 30$ μHz. Our method achieves a travel-time accuracy of 8 ms for the order of discretization 10 (Fig. 8), with or without the presence of a background meridional flow [see 3]. This result can be improved up to 1 ms if we use order 12, which is ~50% more computationally expensive.

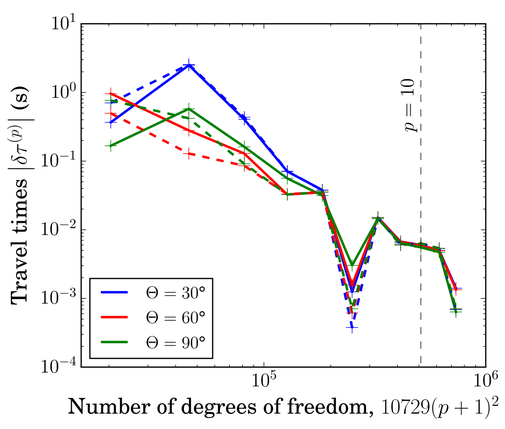

Figure 8: Travel times induced by using a lower order of discretization p. Dashed and solid lines indicate respectively simulations with and without background flow.

Accuracy of Flow Kernels. Figure 9 shows a simplified case of kernels defined in Eq. (10) for a meridional flow, where the kernels for flow components K_{u_r} and K_{u_θ} are azimuthally averaged $\left[\langle K_{u_r}\rangle, \langle K_{u_\theta}\rangle\right]$. Here, we compare the travel time differences induced by a meridional flow cell through forward modelling as well as using Eq. (5). We find that the accuracy of our kernels is of the order 10^{-3} s. This is an important result, as it demonstrates that our kernels have sufficient accuracy for the interpretation of solar travel times. For meridional circulation measurements, the noise in the travel times is typically of order 0.1-0.5 s [4] .

When the two sources are off-axis, the azimuthally averaged kernels require the computation of many components $\langle K\rangle_m$. Figure 10 shows the components of flow kernel for all $m \leq 35$. To test the convergence in m of these kernels, we calculate individual kernels including all modes $|m| \leqslant m_{\rm max}$ and compute travel times as a function of $m_{\rm max}$ in the presence of the same meridional flow as used previously. Travel times converge to an asymptotic value for $m_{\rm max} > 25$ with an accuracy of ~ 0.01 s. We note that a larger $m_{\rm max}$ is needed to achieve convergence for shorter separation distances.

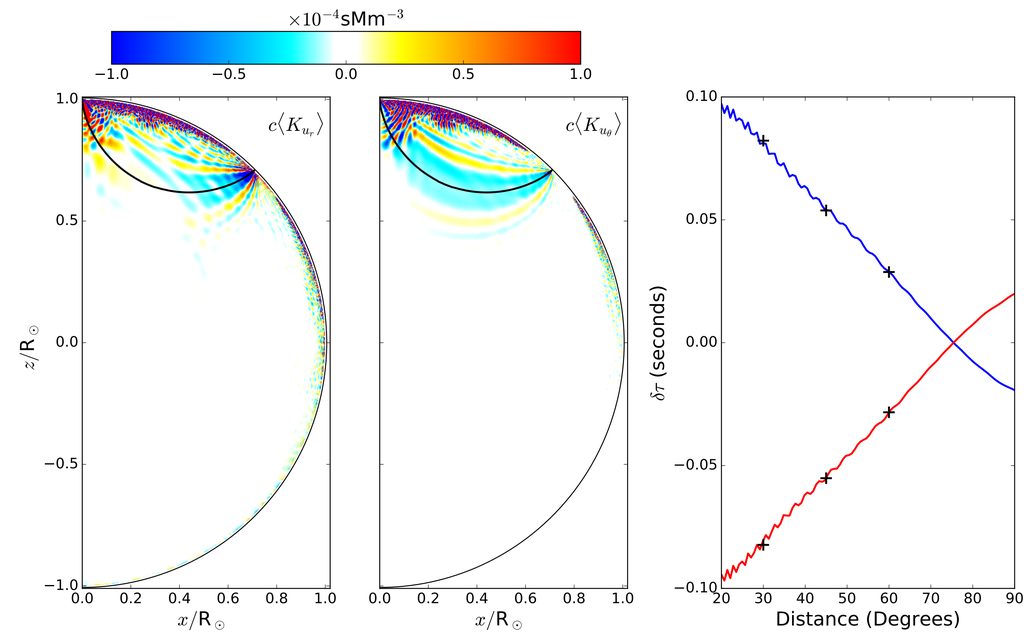

Figure 9: Left and center panels: Kernels $\langle K_{u_r}\rangle$ and $\langle K_{u_\theta}\rangle$ for the r and θ components of the flow. Point $\boldsymbol{r}_1$ is at the north pole (photosphere) and point $\boldsymbol{r}_2$ is at $45°$ latitude. The values of the kernels are scaled by the sound speed c and are saturated at $1/600$-th of the maximum value. The ray-path connecting the two points is shown (thick black line) as well as the computational boundary (black half circle). Right panel: Comparisons of the travel times computed directly from the cross-covariance function and computed from the kernels (black crosses). The travel times in the forward modelling are measured from the pole to latitude $45°$ (blue curve), and in the opposite direction (red curve). The accuracy of the travel times is of order 10^{-3} s.

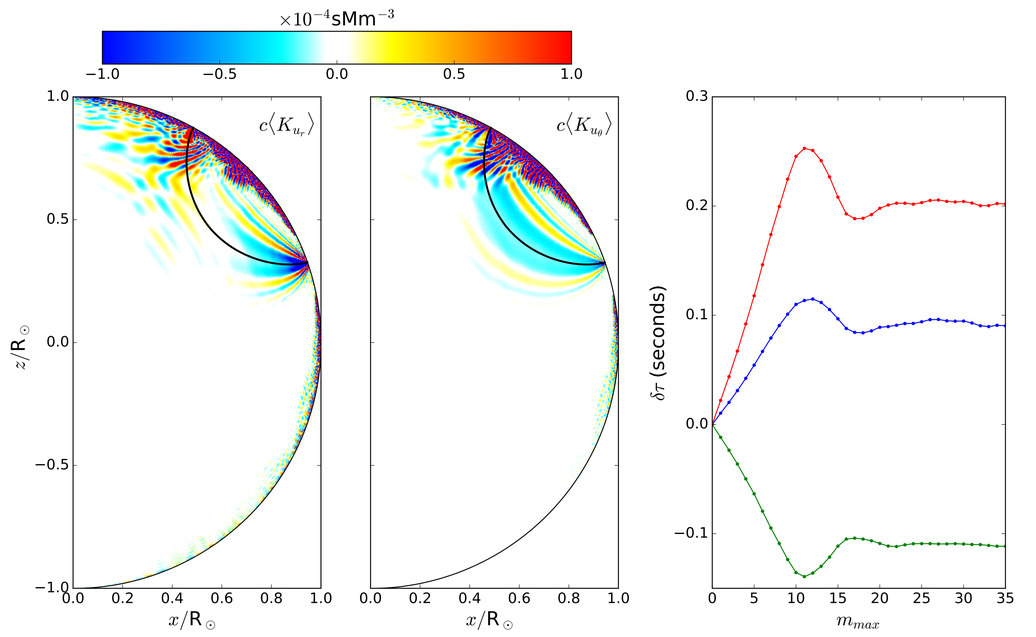

Figure 10: Left and center panels: Kernels $\langle K_{u_r}\rangle$ and $\langle K_{u_\theta}\rangle$ for the r and θ components of the flow, using all azimuthal components $|m| \leq m_{\rm max} = 35$. Point $\boldsymbol{r}_1$ is at latitude $61°$ and point $\boldsymbol{r}_2$ at $19°$. The separation distance between points $\boldsymbol{r}_1$ and $\boldsymbol{r}_2$ is $42°$ with the center point located at a latitude of $40°$. The ray path connecting the two points is shown in black, and reaches a depth of $0.72\ R_\odot$.
Right panel: convergence of the travel times as a function of $m_{\rm max}$, for the North-South (blue) and South-North (green) travel directions. The red curve shows their difference.

A new BC to improve computational efficiency.

A major drawback of the atmosphere extension is that it requires a very high number of mesh cells above the solar surface. Here we introduce a radiating BC that simulates the presence of an atmosphere in which the sound speed is constant, and the density exponentially decaying, without adding any layers to the original mesh. The derivation of this BC at different orders is detailed in [1]. Here we tested the first order BC, that is:

$$\partial_{\boldsymbol{n}} G_\omega = \frac{1}{2H} G_\omega + \frac{\mathrm{i}\omega}{c} \sqrt{1 - \frac{c^2}{4H^2\omega^2}}\, G_\omega \text{ on } S, \qquad (15)$$

where H is the density scale height at the end of model S. Note that the two BCs are equivalent in a uniform background.

Table: Requirements for a single $m - \omega$ Green's function. Note that a full 3D Green's function computation typically requires more than 3 600 frequencies and about 150 m modes to produce accurate kernels.

BC	Mesh cells	CPU Time	Memory
(12)	10 729	199 s	10.1 GB
(15)	5 097	91 s	5.0 GB

References

[1] H. Barucq, J. Chabassier, M. Duruflé, and L. Gizon. Atmospheric radiation boundary conditions for the helmholtz equation. 2016. to be submitted.

[2] L. Gizon and A. C. Birch. Time-distance helioseismology: the forward problem for random distributed sources. *The Astrophysical Journal*, 571:966–986, 2002.

[3] L. Gizon, H. Barucq, M. Duruflé, C. S. Hanson, M. Leguèbe, A. C. Birch, J. Chabassier, D. Fournier, and T. Hohage. Computational helioseismology in the frequency domain: acoustic waves in axisymmetric solar model with flows. 2016. to be submitted.

[4] S. P. Rajaguru and H. M. Antia. Meridional Circulation in the Solar Convection Zone: Time-Distance Helioseismic Inferences from Four Years of HMI/SDO Observations. *Astrophys. J.*, 813:114, November 2015.